EES Batteries

PAPER

View Article Online
View Journal

Cite this: DOI: 10.1039/d6eb00014b

Common-ion driven self-assembly of Cu nanoparticles for interfacial stabilization of Zn anodes

Jooyoung Jang,[a] Yeonwoo Jeong[b] and Changshin Jo *[a,b]

Constructing uniform electrochemically active sites and chemically robust interphases is essential to mitigate the interfacial degradation of Zn anodes in mildly acidic electrolytes. Herein, a self-assembled Cu layer is formed on a Zn electrode *via* a galvanic replacement reaction driven by the reduction potential difference. Unlike conventional physical coatings, this strategy leverages a common-ion effect to finely regulate redox kinetics and control nanoparticle nucleation and growth behavior, leading to the formation of a conformal and densely packed Cu layer without the need for external energy input. This chemically guided Cu layer effectively modulates the surface energy and Zn^{2+} ion flux, resulting in preferential Zn nucleation, and suppresses parasitic byproduct formation. Electrochemical analyses reveal that the Cu-coated Zn anodes can improve cycling stability, with symmetric Zn||Zn cells maintaining stable operation for over 1150 hours and asymmetric Zn||Cu cells operating for more than 1800 hours at 1 mA cm^{-2}, with high coulombic efficiency. Moreover, the preferential (002) orientation and the *in situ* formation of a Cu–Zn alloy enable lower nucleation barriers and promote uniform Zn deposition. This synergistic combination of structure and interfacial properties highlights a promising strategy for interfacial regulation in high-performance Zn-based energy storage systems.

Received 19th January 2026,
Accepted 4th March 2026

DOI: 10.1039/d6eb00014b

rsc.li/EESBatteries

Broader context

The ion-mediated galvanic replacement strategy enables the formation of a conformal Cu nanoparticle interface on Zn anodes, which stabilizes the electrodes during storage and guides uniform Zn growth. Beyond enhancing full-cell stability and efficiency, this concept underscores a versatile pathway for interfacial engineering in aqueous Zn-ion batteries and related electrochemical systems.

Introduction

Aqueous zinc-ion batteries (AZIBs) have emerged as promising next-generation energy storage systems due to the natural abundance and high gravimetric and volumetric capacities (820 mA h g^{-1} and 5855 mA h cm^{-3}) of Zn metal, along with the inherent safety of aqueous electrolytes.[1–4]

However, the electrochemical reversibility of AZIBs is significantly hindered by parasitic reactions and structural instability at the Zn anode interface.[5,6] Zn metal inherently forms non-uniform surface oxide layers during manufacturing, resulting in heterogeneous surface chemical/morphological properties and poor reaction selectivity which lead to an uneven Zn stripping and plating process.[7,8] This limitation is particularly critical in AZIBs, which begin operation with the Zn stripping process. In such discharge-initiated systems, the inherent surface heterogeneity of the Zn anode directly governs the initial dissolution behavior, thereby influencing the uniformity and reversibility of subsequent electrochemical reactions. Moreover, the standard reduction potential of Zn^{2+}/Zn (−0.76 V *vs.* the standard hydrogen electrode, SHE) is more negative than that of the H^+/H_2 couple, rendering Zn metal thermodynamically prone to parasitic corrosion coupled with the hydrogen evolution reaction (HER).[9] This results in localized alkalization at the electrode–electrolyte interface due to the OH^- accumulation associated with HER, accelerating chemical corrosion.[10,11] The accumulated OH^- ions can subsequently react with Zn^{2+} ions and anions (*e.g.*, SO_4^{2-} in $ZnSO_4$ electrolyte) to precipitate zinc hydroxide sulfate ($Zn_4SO_4(OH)_6{\cdot}xH_2O$, ZHS) byproducts, which increase interfacial resistance and accelerate electrode degradation.[12,13]

[a]*Department of Battery Engineering, Graduate Institute of Ferrous & Eco Materials Technology, Pohang University of Science and Technology (POSTECH), 77 Cheongam-ro, Nam-gu, Pohang, Gyeongbuk, 37673, Republic of Korea.*
E-mail: jochangshin@postech.ac.kr
[b]*Department of Chemical Engineering, Pohang University of Science and Technology (POSTECH), 77 Cheongam-ro, Nam-gu, Pohang, Gyeongbuk, 37673, Republic of Korea*

Furthermore, chemical corrosion amplifies current inhomogeneity, concentrating electron flux at surface protrusions. This results in a progressively reduced electrochemically active surface area, promotes dendritic growth, and accelerates localized electrochemical corrosion.[14,15]

Electrolyte-level strategies—such as tuning zinc salts,[16,17] incorporating functional additives,[8,18,19] and introducing redox mediators[20–22]—have been explored to address the aforementioned issues. However, among these approaches, direct interfacial modification of the Zn metal surface is particularly effective because it regulates the local electric field and interfacial chemistry at the source. A widely employed strategy to tackle the abovementioned issues involves applying artificial protective coatings, including inorganic composite films (*e.g.*, TiO_2,[13,23] Al_2O_3,[24] and MOFs[25,26]), which help regulate charge distribution and suppress parasitic reactions. However, these inorganic layers often exhibit weak interfacial adhesion to the Zn substrate and are prone to cracking or delamination under repeated volume fluctuations during Zn stripping/plating. Given these challenges, one widely investigated approach is the alloying of Zn with foreign metals such as Ag,[27,28] In,[29,30] Sn,[31,32] or Cu,[33] which provides robust interfacial contact together with reduced interfacial energy and improved corrosion resistance. Nevertheless, conventional alloying strategies would require careful control of alloy composition, and the synthesis process could be sensitive to processing parameters, which can pose challenges for reproducibility. In this work, we propose a spontaneous interfacial engineering strategy that enables *in situ* self-assembly of uniformly distributed Cu nanoparticles (NPs) on a Zn electrode *via* a galvanic replacement reaction with Cu^{2+} ions. To further tune the redox kinetics and nucleation behavior, $ZnSO_4$ was incorporated to induce a common-ion effect. In this process, the excess Zn^{2+} and SO_4^{2-} ions act through the common-ion effect to shift the equilibrium of the galvanic replacement reaction, effectively lowering the thermodynamic driving force for Cu^{2+} reduction. This ion-mediated regulation slows nucleation kinetics, leading to a dense and evenly distributed Cu NP layer without the need for high-temperature annealing or vacuum deposition. A self-assembled Cu NP layer on the Zn electrode, formed by immersion in 1 M $ZnSO_4$ + 0.05 M $CuSO_4$ (ZSCS) solution, effectively facilitates uniform nucleation and suppresses local electric field intensification. In Zn‖Cu half-cells, the ZSCS electrode sustained stable cycling performance for over 1800 hours with a superior average coulombic efficiency (CE) of 99.8%, whereas the bare Zn cell experienced internal shorting within 400 hours. The formation of Cu–Zn alloy phases after cycling may have enhanced reversibility by stabilizing the electrode–electrolyte interface and mitigating side reactions during repeated Zn plating and stripping processes. Notably, in full-cell systems using sodium vanadate (NVO) cathodes, *in situ* X-ray diffraction (XRD) patterns revealed that ZHS formation on the cathode was mitigated when coupled with ZSCS anodes, which is likely attributed to the stabilized interfacial behavior of the modified anode influencing the overall cell environment during the initial cycle. This interfacial regulation resulted in 83.8% capacity retention for the NVO‖ZSCS full cell at 1 A g^{-1} with an average CE of 99.6% over 100 cycles, pointing to the potential of this interfacial engineering strategy for durable aqueous Zn-based batteries.

This study shows that combining spontaneous galvanic replacement with ion-mediated modulation of interfacial redox behavior is an effective strategy for improving the electrochemical stability and reversibility of Zn metal anodes. This approach not only suppresses uncontrolled reaction dynamics but also highlights the potential of ionic environment control as a tool for interfacial design.

Results and discussion

Common-ion effect in regulating Cu nucleation behavior

A spontaneous redox reaction between Zn and Cu^{2+} is driven by their difference in standard reduction potentials (−0.76 V for Zn^{2+}/Zn and +0.34 V for Cu^{2+}/Cu *vs.* the SHE). When Zn metal is immersed in a $CuSO_4$ solution, Zn is oxidized to Zn^{2+}, while Cu^{2+} ions are reduced and deposited as metallic Cu on the Zn surface. This galvanic replacement occurs spontaneously at room temperature without external energy input (Fig. 1a). In this experiment, Zn foil was immersed in 0.05 M $CuSO_4$ (CS) solution to fabricate a Cu layer on a Zn electrode (Fig. 1b, left). Under these conditions, the fast reduction of Cu^{2+} induced uncontrolled nucleation, yielding coarse and irregular Cu particles with severe aggregation on the Zn surface, as confirmed by scanning electron microscopy (SEM) analysis (Fig. 1c). To obtain a uniform Cu NP assembly, we applied a design principle derived from electroless plating, which emphasizes precise precursor concentration control and homogeneous solution conditions under unbiased environments.[34] In line with this concept, the introduction of $ZnSO_4$ salts (Fig. 1b, right) induced a common ion effect that shifts the solubility equilibrium and moderates the redox and nucleation behavior of Cu^{2+}. At its core, the common ion effect operates through two main mechanisms: (i) reduction of the thermodynamic driving force and (ii) regulation of Cu^{2+} activity. In terms of Zn^{2+} ion concentration, an increased Zn^{2+} ion activity reduces the electrochemical driving force, as described by the Nernst equation,[35,36] meaning that Zn oxidation becomes less favorable and the coupled Cu^{2+} reduction is consequently suppressed. From a chemical equilibrium perspective, this behavior can also be interpreted through the common ion effect, where excess Zn^{2+} shifts the Zn^{2+}/Zn equilibrium toward the solid phase, reducing the thermodynamic tendency for Zn dissolution. In parallel, excess SO_4^{2-} ions can strengthen the solvation structure of Cu^{2+}, thereby slowing its desolvation and modulating nucleation kinetics. A more detailed discussion of the kosmotropic nature of SO_4^{2-} will be provided in a subsequent section. This dual effect creates a self-limiting environment that favors the formation of uniformly distributed and conformal Cu NPs on the Zn surface.

Consistent with this mechanism, SEM analysis confirmed the formation of a compact and homogeneous Cu NP layer on

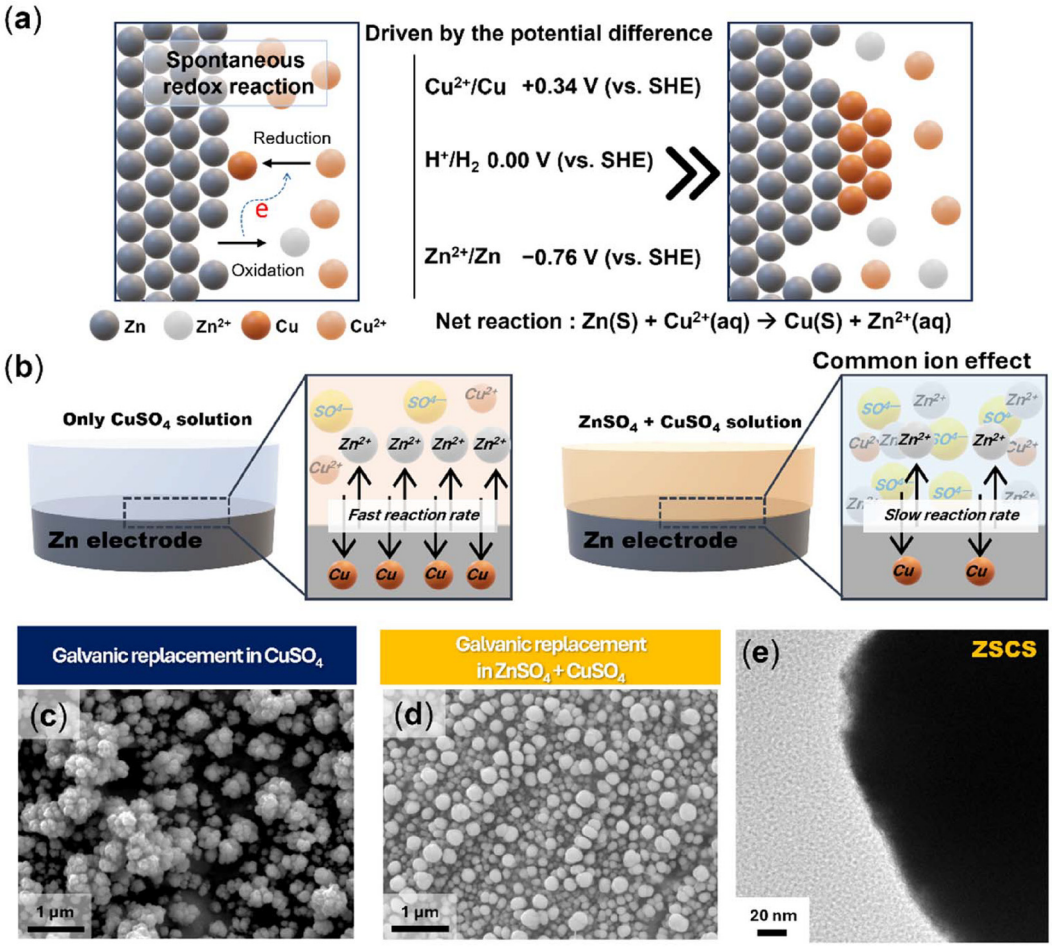

Fig. 1 (a) Schematic illustration of the galvanic replacement between Zn metal and Cu^{2+} ions. (b) Schematic representation of Cu nucleation modulated by the common-ion effect. Top-view scanning electron microscopy (SEM) images of Cu coatings obtained in (c) 0.05 M $CuSO_4$ (CS) and (d) 0.05 M $CuSO_4$ + 1 M $ZnSO_4$ (ZSCS) solutions. (e) Transmission electron microscopy image of a Cu particle formed under the ZSCS condition.

the Zn electrode immersed in ZSCS solution (Fig. 1d). Transmission electron microscopy analysis further confirmed that the Cu NPs formed under the ZSCS condition possess well-defined surfaces with minimal oxide layers (Fig. 1e). In addition, cross-sectional SEM analysis revealed clear morphological contrast between CS- and ZSCS-treated electrodes. The CS-treated electrode showed a loosely packed and poorly covered Cu layer (Fig. S1b), while the ZSCS electrode formed a conformal and well-integrated coating on Zn (Fig. S1c). The top-view SEM image and energy dispersive X-ray spectroscopy (EDS) mapping, and cross-sectional EDS mapping further confirmed a Cu-rich surface layer on Zn with a clear Cu/Zn interface. Since the bare Zn substrate was highly rough (Fig. S1a), the galvanic replacement coating followed the local topography, leading to position-dependent thickness. Nevertheless, under ZSCS, the coating became more conformal and continuous with reduced thickness inhomogeneity compared to CS, and the average thickness was ~1 μm (Fig. S2). Moreover, optical characterization displayed a distinct difference: the CS-treated Zn appeared dark black due to aggregated Cu particles with strong light absorption, while ZSCS-treated Zn exhibited a brighter grayish-yellow colour, consistent with a compact Cu coating that enhances reflectivity (Fig. S3).[37,38] Collectively, these morphological and optical features exhibit the effectiveness of the common ion-mediated strategy in producing a uniform and robust interfacial Cu layer.

In this context, $CuSO_4$ precursor concentration is another key factor that critically influences Cu particle formation. At 0.01 M, sluggish reduction kinetics yielded negligible Cu deposition, whereas at 0.1 M, excessive reduction led to rapid nucleation and severe particle coalescence (Fig. S4). These results indicate that an overabundance of free Cu^{2+} ions can overwhelm the $ZnSO_4$-based common ion effects. Therefore, we chose the ZSCS condition as the optimum, as it balances common-ion regulation with controlled $CuSO_4$ concentration to produce a uniform and reproducible Cu coating. Cu nucleation on the Zn surface is strongly affected by the desolvation kinetics of Cu^{2+}. Since these kinetics are intrinsically governed by the surrounding solvation structure, the influence of SO_4^{2-} on hydrogen-bonding networks was investigated using Fourier-

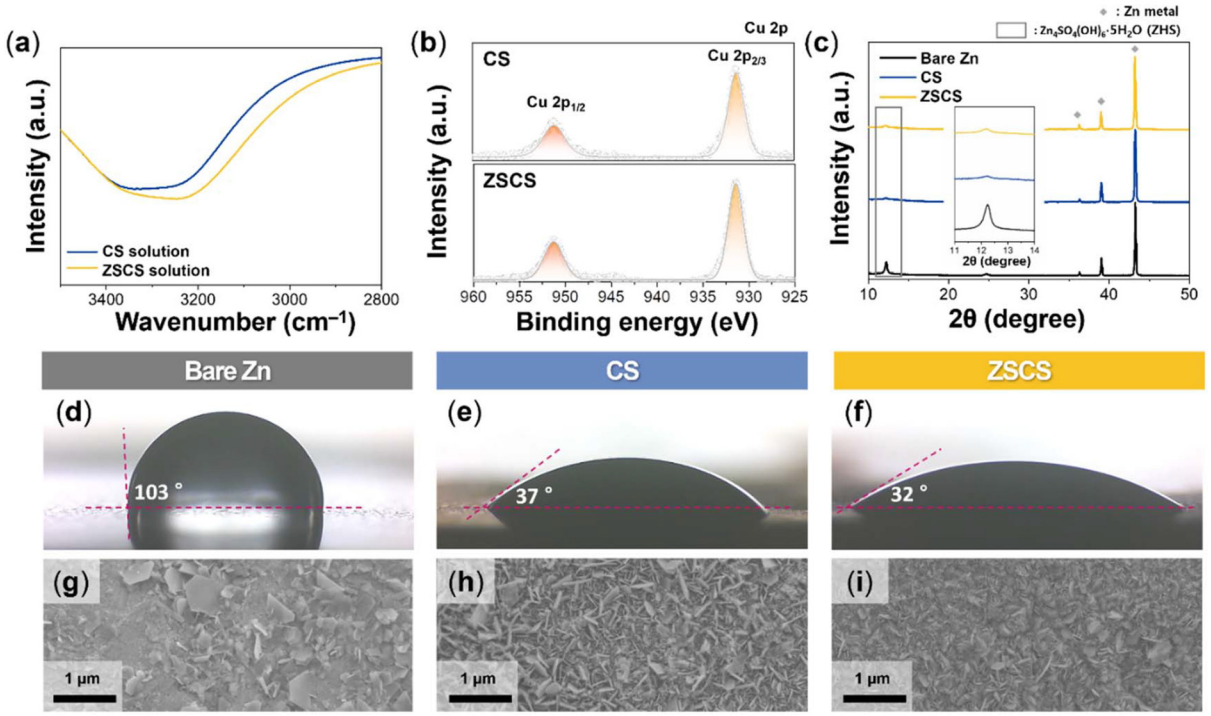

Fig. 2 (a) Fourier-transform infrared spectroscopy spectra of CS and ZSCS solutions. (b) Cu 2p X-ray photoelectron spectroscopy spectra of CS and ZSCS electrodes. (c) X-ray diffraction (XRD) patterns of Zn electrodes after 6 h soaking in 2 M $ZnSO_4$. (d–f) Contact angle measurements of bare Zn, CS, and ZSCS surfaces. (g–i) Top-view SEM images of the corresponding electrodes after 6 h immersion in 2 M $ZnSO_4$.

transform infrared (FTIR) spectroscopy (Fig. 2a). In the O–H stretching vibration region (3200–3600 cm^{-1}), the ZSCS solution exhibited a distinct red-shift and band broadening compared with the CS condition, indicative of strengthened hydrogen bonding between SO_4^{2-} anions and water molecules. This observation is consistent with the kosmotropic nature of SO_4^{2-} described in the Hofmeister series, wherein enhanced hydrogen-bond structuring reduces bulk water activity. Such restructuring of the aqueous environment is expected to suppress Cu^{2+} desolvation, thereby moderating the kinetics of the galvanic replacement reaction and effectively lowering nucleation rates while minimizing particle coalescence.

To investigate the chemical state of deposited Cu, X-ray photoelectron spectroscopy (XPS) analysis of the Cu 2p region was conducted for both CS and ZSCS conditions (Fig. 2b). In both cases, the Cu 2p spectra are well reproduced by a single constrained Cu $2p_{3/2}$–Cu $2p_{1/2}$ doublet without noticeable shoulder components with main peaks at ≈932.6 eV (Cu $2p_{3/2}$) and ≈952.4 eV (Cu $2p_{1/2}$), indicating the presence of metallic Cu^0.[39,40] The absence of shake-up satellite peaks (941–945 eV) suggests negligible formation of Cu(II) species.[41] These results support that spontaneous galvanic replacement can yield metallic Cu on the Zn surface.

Zn metal in a $ZnSO_4$-based aqueous electrolyte directly reacts with Zn^{2+}, SO_4^{2-}, and OH^- to form ZHS byproducts, which can hinder charge transfer and trigger heterogeneous interfacial reactions. XRD analysis of bare Zn electrodes immersed in 2 M $ZnSO_4$ for 6 h revealed a strong diffraction peak at ≈12.3°, corresponding to the (001) plane of water-deficient ZHS (Fig. 2c).[42] In contrast, this peak intensity was markedly decreased under CS and ZSCS conditions, implying that byproduct formation was suppressed. These results suggest that the Cu layer can inhibit direct interaction between Zn and reactive electrolyte species, thereby improving interfacial stability.

Furthermore, electrochemical impedance spectroscopy spectra showed that the bare Zn symmetric cell after 6 h of rest exhibited higher charge transfer resistance than the cells with CS and ZSCS electrodes (Fig. S5). This result indicated that the Cu-modified interface suppresses spontaneous ZHS formation, thereby preserving interfacial conductivity and improving storage stability prior to electrochemical cycling.

Inhomogeneous ZHS formation may originate from poor electrolyte wettability of Zn electrodes, which promotes uneven electrolyte spreading and localized pH fluctuations.[8] As observed in the SEM image (Fig. S6), bare Zn exhibits an irregular and rough surface morphology, which can promote a heterogeneous local current distribution and interfacial reactions. Contact angle measurements using 2 M $ZnSO_4$ showed that bare Zn exhibited a high angle of 103°, indicative of hydrophobicity (Fig. 2d). In contrast, CS and ZSCS electrodes displayed much lower angles (37° and 32°, respectively), reflecting the improved electrolyte affinity introduced by the Cu layer (Fig. 2e and f and S7).[43,44] The further reduction observed for ZSCS is likely associated with the more uniform and conformal Cu coating formed under the common-ion effect, which promotes enhanced electrolyte

spreading. Top-view SEM images of the Zn electrode immersed in electrolyte for 6 h supported these findings: bare Zn showed deposition of large and plate-like ZHS crystals with unreacted regions, while the CS electrode exhibited smaller and less aggregated particles (Fig. 2g and h). Notably, the ZSCS electrode displayed minimal ZHS presence, confirming the Cu layer's role in suppressing byproduct nucleation and promoting interfacial homogeneity (Fig. 2i). To further assess the interfacial stability in aqueous media, the HER was evaluated *via* linear sweep voltammetry (Fig. S8). At −10 mA cm^{-2}, the potential was −1.78 V for bare Zn, −1.83 V for CS, and −1.86 V for ZSCS, indicating that the Cu layer shifts the HER onset to more negative values and enhances interfacial stability by suppressing parasitic hydrogen evolution.[45]

Regulating initial Zn deposition for stable interfaces

To determine the role of Cu-coated Zn electrodes in regulating current distribution and improving the interfacial stability during Zn plating and stripping processes, both symmetric and half-cell configurations were employed: a Zn‖Zn symmetric cell configuration to examine the Zn deposition behavior *via* chronoamperometry and a Zn‖Cu asymmetric cell configuration to assess the Zn stripping characteristics during the discharge process. Fig. 3a presents the chronoamperometry results from the Zn‖Zn symmetric cell configuration at a constant overpotential of −150 mV. The symmetric cell with bare Zn electrodes (bare Zn‖bare Zn) showed a sharp initial current spike followed by a gradual increase, reflecting interfacial instability caused by localized Zn^{2+} depletion and non-uniform deposition. This behavior is characteristic of the Sand's time phenomenon, where diffusion breakdown triggers dendritic growth under steep concentration gradients.[46,47]

In contrast, the asymmetric cell (bare Zn‖ZSCS), where Zn plating occurred on the ZSCS electrode, maintained a stable current response, confirming that the surface modification effectively stabilizes the Zn plating process (Fig. S9).

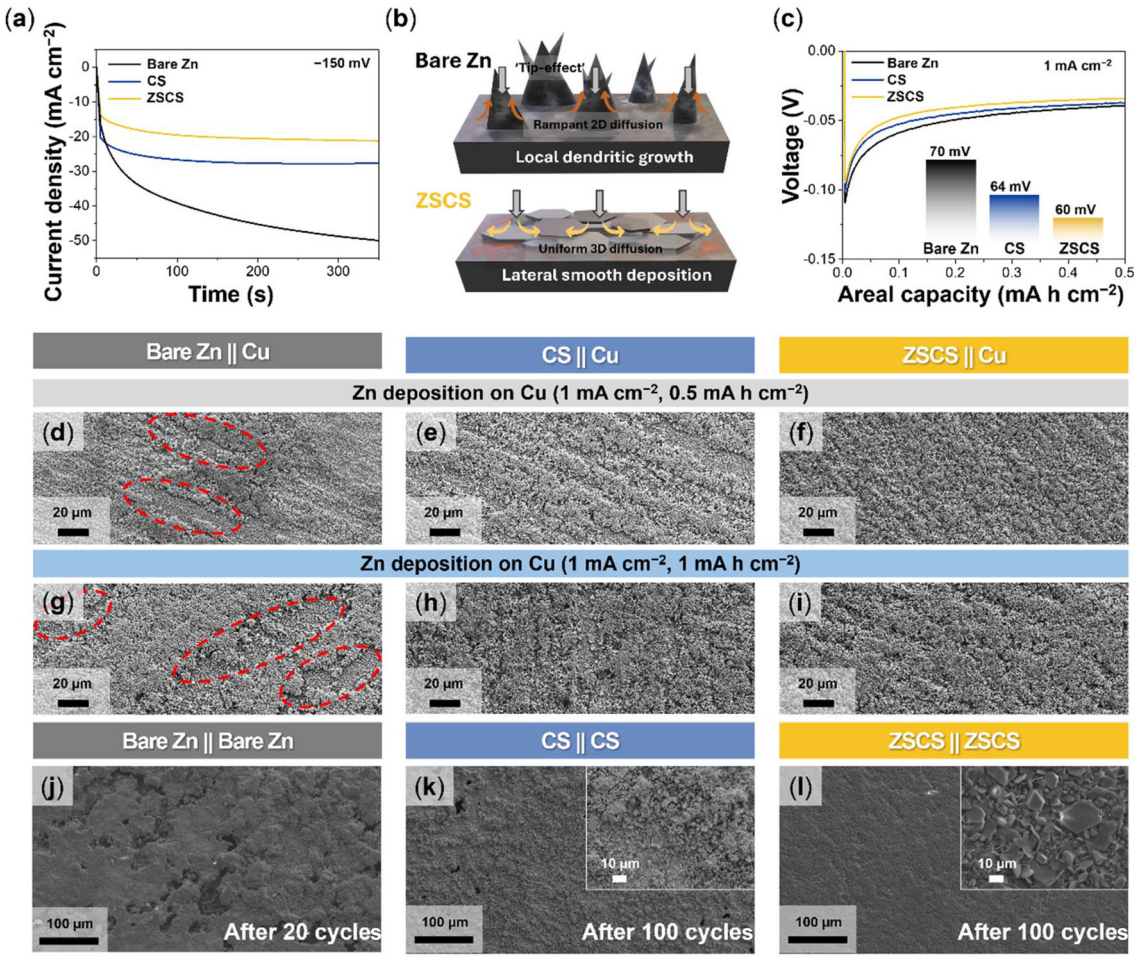

Fig. 3 (a) Chronoamperometry results of Zn‖Zn symmetric cells under a constant overpotential of −150 mV. (b) Schematic illustration comparing the Zn deposition behavior between bare Zn and ZSCS-modified Zn electrodes. (c) Voltage profiles of Zn‖Cu half-cells at 1 mA cm^{-2}. Top-view SEM images of Cu electrodes after Zn plating at 1 mA cm^{-2} and 0.5 mA h cm^{-2} using (d) bare Zn, (e) CS, and (f) ZSCS anodes. Top-view SEM images of Cu electrodes under increased plating capacity (1 mA h cm^{-2}), showing Zn deposition from (g) bare Zn, (h) CS, and (i) ZSCS. The surface morphology of Zn electrodes in Zn symmetric cells: (j) the bare Zn electrode after only 20 cycles and (k) CS and (l) ZSCS electrodes after 100 cycles at 1 mA cm^{-2} with 1 mA h cm^{-2}.

Furthermore, the fully symmetric configuration (ZSCS||ZSCS) exhibited the lowest and most stable current density, highlighting the superior interfacial stability achieved when both electrodes were modified. As depicted in Fig. 3b, while the bare Zn surface promotes vertical dendritic growth *via* tip-induced 2D diffusion, the ZSCS electrodes enable lateral and homogeneous deposition through a more uniform 3D diffusion pathway guided by the self-assembled Cu layer.[48] Further insight into interfacial kinetics was obtained from activation energy (E_a) analysis from Arrhenius plots (Fig. S10). The cells with CS and ZSCS electrodes exhibited lower E_a values (20.1 and 21.4 kJ mol^{-1}, respectively) compared to bare Zn (34.3 kJ mol^{-1}). The Cu-modified surfaces lower the energy barrier for Zn^{2+} desolvation and nucleation, thereby improving interfacial charge transfer capability.[49,50]

The influence of the initial Zn stripping behavior and its effect on Zn^{2+} nucleation at the counter electrode was shown using Zn||Cu half-cell configurations. As shown in the discharge profiles (Fig. 3c), the ZSCS||Cu configuration cell exhibited the lowest nucleation overpotential (≈60 mV) than that with bare Zn (≈70 mV) and CS (≈64 mV) electrodes due to the well-regulated Cu layer morphology in the ZSCS system. This electrochemical behavior is directly correlated with the observed deposition morphology on the Cu counter electrodes.

At a current density of 1 mA cm^{-2}, SEM images revealed that the bare Zn electrode induced a non-uniform Zn deposition on Cu counter electrodes, forming irregular clusters with large inactive areas (Fig. 3d). This deposition heterogeneity, consistent with the chronoamperometry results of the bare Zn symmetric cell, may be attributed to the intrinsic surface roughness of bare Zn (Fig. S6) that causes uneven local current density. In contrast, both CS- and ZSCS-modified electrodes promoted a more uniform Zn deposition across the Cu electrode surface (Fig. 3e and f). Particularly, the ZSCS-modified electrode exhibited a dense and continuous deposition layer even at a high areal capacity of 1 mA h cm^{-2} (Fig. 3g–i). These results suggest that the Cu NP layer can guide uniform Zn stripping and Zn^{2+} ion flux owing to its role in reducing interfacial heterogeneity and maintaining a homogeneous diffusion pathway.

The Zn deposition morphology upon prolonged cycling further corroborates the effect of the Cu coatings. After just 20 cycles, the bare Zn electrode from the Zn||Zn symmetric cell showed severe surface degradation, characterized by surface collapse and severe pitting (Fig. 3j). In contrast, both CS and ZSCS electrodes retained relatively smooth surfaces even after 100 cycles, with notably mitigated pitting (Fig. 3k and l). Particularly, the ZSCS-modified electrode exhibited a preferred Zn crystal growth along the (002) plane of Zn (Fig. 3l, inset). This observation is further supported by the 70°-tilted SEM images and atomic force microscopy topography (Fig. S11 and S12), which reveal a more continuous and compact deposition layer with reduced out-of-plane roughness compared to the CS electrode. Such facet-selective growth helps suppress tip effects and Zn^{2+} ion flux localization, offering enhanced interfacial stability and prolonged Zn anode lifespan.

The initial differences in Zn stripping and plating behavior observed in Zn asymmetric and symmetric cell configurations directly influence long-term electrochemical reversibility. In Zn||Cu cells, the bare Zn electrode failed after 202 cycles due to internal short-circuit, whereas the ZSCS electrode remained stable for over 1800 hours with a high average CE of 99.8% (Fig. 4a and S13). This remarkable durability arises from the Cu NP coating, where uniform Zn stripping induces compact redeposition on the Cu counter electrode, mitigating interfacial degradation. In Zn||Zn symmetric cells at 1 mA cm^{-2} and 1 mA h cm^{-2}, the bare Zn electrode showed a high initial overpotential with a nucleation overpotential of 72 mV (Fig. 4b). Moreover, a voltage spike was observed during Zn redeposition on the previously stripped bare Zn electrode. Previous studies report that this behavior suggests non-uniform stripping-induced surface inhomogeneity with pits and roughness, which increases the local nucleation barrier and leads to a non-uniform current distribution during subsequent deposition.[51,52]

Meanwhile, the CS and ZSCS electrodes exhibited significantly lower overpotentials (≈36–37 mV) without noticeable voltage fluctuations, implying more uniform Zn dissolution and redeposition behavior and improved Zn^{2+} nucleation kinetics. These improvements in electrochemical reversibility are consistent with previous reports, which showed that Cu possesses an optimal binding energy with Zn (approximately −0.99 eV)—strong enough to promote uniform Zn nucleation, yet sufficiently moderate to enable efficient stripping.[53]

The rate capability was evaluated in Zn||Zn symmetric cells with progressively increasing the current densities from 0.5 to 10 mA cm^{-2} and with a constant areal capacity of 1 mA h cm^{-2} (Fig. 4c). The cell with bare Zn underwent an internal short circuit even at 1 mA cm^{-2}, indicating poor interfacial stability under moderate cycling conditions. In contrast, both CS and ZSCS electrodes maintained stable operation even at high current densities up to 10 mA cm^{-2}, highlighting improved interfacial robustness and reversibility of Cu-modified electrodes under harsh operating conditions.

Long-term cycling tests at 1 mA cm^{-2} with a fixed areal capacity of 1 mA h cm^{-2} further confirmed this performance distinction (Fig. S14). The bare Zn electrode failed after only ≈88 hours, while the CS and ZSCS electrodes operated stably for ≈717 and ≈762 hours, respectively, showing the effectiveness of the surface modification in prolonging Zn anode lifespan. Notably, the ZSCS electrode further exhibited remarkable long-term stability under varying operating conditions, maintaining stable cycling for over 740 hours at 2 mA cm^{-2} with 1 mA h cm^{-2} and exceeding 1150 hours at 1 mA cm^{-2} with 0.5 mA h cm^{-2} (Fig. 4d and e).

This long-term electrochemical stability implies a favorable Zn deposition behavior, which is further supported by structural evidence obtained from post-cycling XRD analysis. The ZSCS electrode from the cell after 20 cycles exhibited a notably higher (002)/(100) peak intensity ratio of 1.1 compared to CS and bare Zn (Fig. 4f). This preferential orientation along the (002) plane suggests a directionally controlled crystal growth

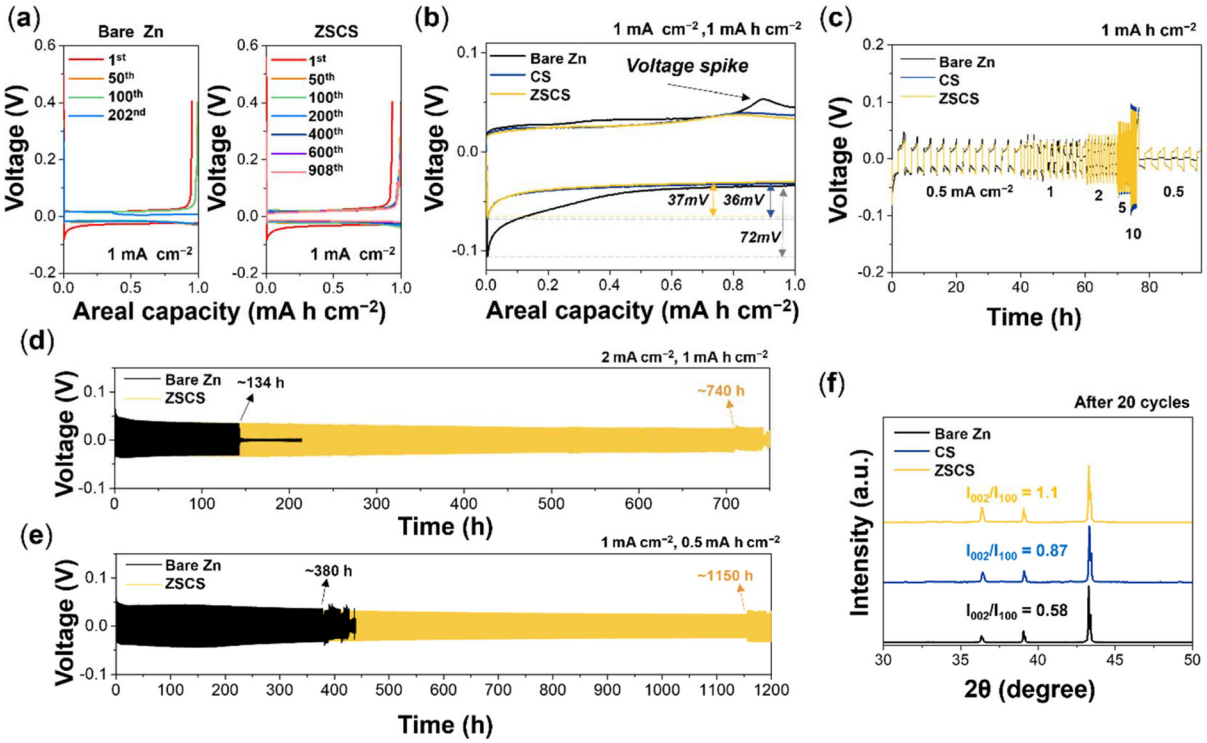

Fig. 4 (a) Voltage profiles of Zn||Cu half-cells with bare Zn and ZSCS anodes at 1 mA cm^{-2}. (b) Voltage profiles of Zn symmetric cells at 1 mA cm^{-2} with 1 mA h cm^{-2}. (c) Rate performance of Zn symmetric cells under stepwise current densities from 0.5 to 10 mA cm^{-2}. Long-term cycling performance at (d) 2 mA cm^{-2} with an areal capacity of 1 mA h cm^{-2} and (e) 1 mA cm^{-2} with an areal capacity of 0.5 mA h cm^{-2}. (f) XRD patterns of Zn electrodes after 20 cycles.

behavior, which aligns with the surface morphology obtained from SEM results. Furthermore, $CuZn_5$-related diffraction peaks are observed in the enlarged XRD profile shown in Fig. 4f (Fig. S15), evidencing *in situ* Cu–Zn alloy formation *via* solid-state diffusion during cycling. This alloying behavior is in line with previous reports,[54–56] featuring lattice matching with the Zn (002) plane. Such epitaxial growth not only promotes uniform Zn plating but also effectively suppresses dendritic growth and interfacial parasitic reactions, thereby contributing to the enhanced electrochemical stability observed in this work.

Full-cell cycling stability with suppressed byproduct formation

To validate the improved electrochemical performance of the self-assembled Cu layer on the ZSCS electrode, full cells were constructed using NVO cathodes paired with either bare Zn or Cu-modified Zn anodes. The NVO nanofibers were synthesized according to a previously reported method.[57] SEM imaging confirmed that the NVO powder exhibits a well-defined particle morphology, and EDS mapping further verified the uniform distribution of Na, V, and O elements, indicating the successful synthesis of NVO (Fig. S16). Cyclic voltammetry profiles of all three full-cell configurations exhibited two pairs of well-defined redox peaks within the voltage range of 0.2–1.6 V at a scan rate of 0.2 mV s^{-1}, indicating reversible charge storage behavior in the NVO cathode (Fig. 5a). Furthermore, the peak separation of the NVO||ZSCS cell (0.185 V) was smaller than that of NVO||bare Zn (0.23 V), suggesting that the Cu NP layer reduces interfacial resistance and enables more reversible Zn redox kinetics. The initial galvanostatic charge/discharge curves at 200 mA g^{-1} showed comparable specific capacities of ≈295 mA h g^{-1} for all three cell configurations, implying that the Cu-modified anode surfaces do not interfere with the electrochemical utilization of the NVO cathode (Fig. 5b).

The modification strategy for the Zn anode should not be evaluated solely based on its local interfacial behavior, but also based on its systemic impact on the cathode side. Specifically, uneven Zn stripping can induce localized pH rises and excess OH^- generation, which subsequently diffuse across the electrolyte and can react with Zn^{2+} species on the cathode side.[58,59] *In situ* XRD analysis determined this mechanism by revealing stronger ZHS signals on the NVO cathode paired with a bare Zn anode, compared to the ZSCS system (Fig. 5c and d). The ZSCS-modified anode promotes uniform Zn stripping, thereby minimizing local pH fluctuation and suppressing ZHS formation, which correlates with the reduced parasitic reactions observed in symmetric and half-cell tests. These findings suggest that anode engineering not only stabilizes Zn deposition but also alleviates cathode-side degradation, advancing anode-focused studies toward a deeper understanding of full-cell chemistry.

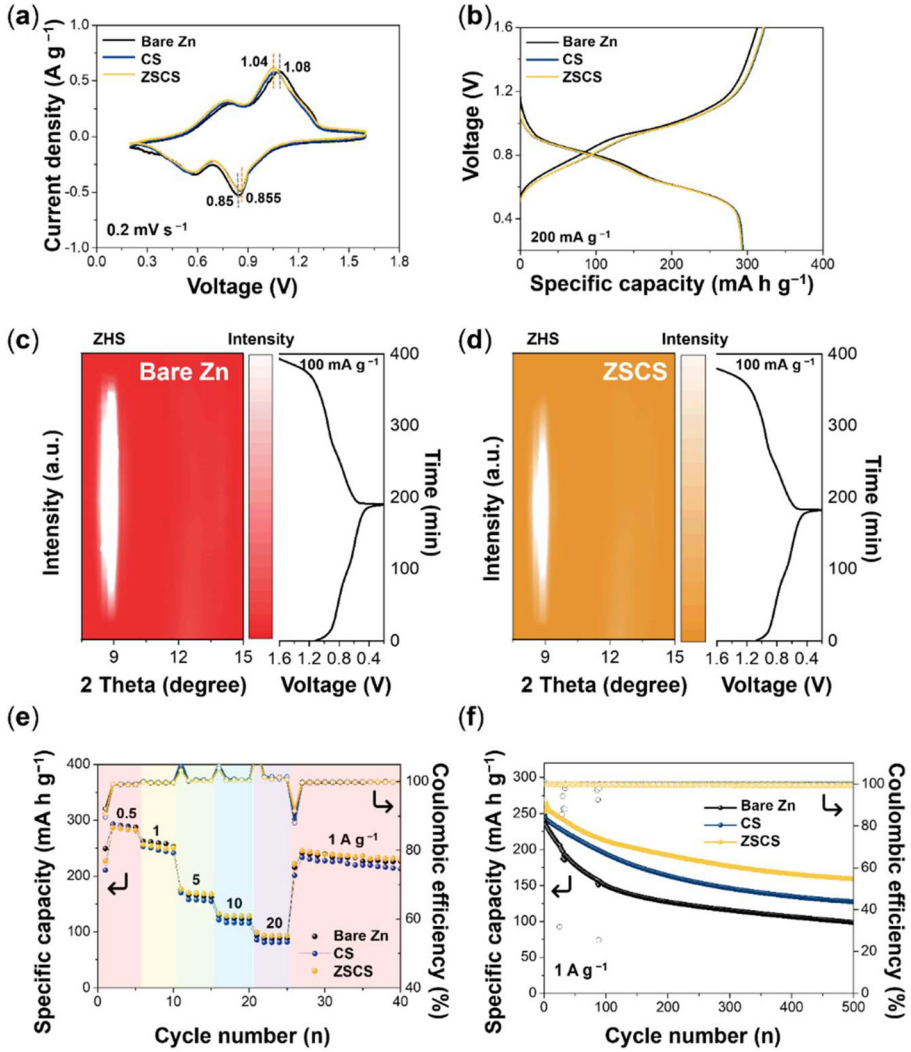

Fig. 5 Electrochemical performance of full cells assembled with bare Zn, CS, and ZSCS anodes and sodium vanadate (NVO) cathodes. (a) Cyclic voltammetry curves at 0.5 mV s^{-1}. (b) Initial galvanostatic charge/discharge profiles at 200 mA g^{-1}. *In situ* XRD analysis reveals ZHS formation on the NVO cathode paired with (c) bare Zn and (d) ZSCS electrodes. (e) Rate performance of the NVO full-cell across current densities of 0.5–20 A g^{-1}. (f) Long-term cycling performance of the NVO full-cell at 1 A g^{-1}.

The rate performance was evaluated by increasing the specific currents ranging from 0.5 to 20 A g^{-1} (Fig. 5e). At high current densities (5–20 A g^{-1}), the ZSCS-modified full cell consistently delivered higher specific capacities than the bare Zn||NVO cell, reflecting the superior charge-transfer kinetics and interfacial stability provided by the self-assembled Cu layer. Notably, when the specific capacity was returned to 1 A g^{-1} after cycling at 20 A g^{-1}, the ZSCS||NVO cell recovered 86.6% of its first specific capacity at 1 A g^{-1}, which further increased to 89.5% by the 40th cycle. In contrast, the bare Zn cell recovered only 82.1% of its original capacity under the same conditions and reached a slightly lower recovery of 86.4% after 40 cycles.

Long-term cycling performance was subsequently examined to evaluate the durability of the Cu-modified electrode. After 100 cycles at 1 A g^{-1}, the ZSCS||NVO cell retained 83.8% of its initial capacity with a high average CE of 99.6%, while the bare Zn||NVO cell exhibited only 62.3% capacity retention despite a comparable CE of 97.7%. Even after 500 cycles, the ZSCS||NVO cell maintained 62.7% of its capacity, outperforming the bare Zn cell, which retained only 41.0% (Fig. 5f). Compared to the CS||NVO system, which showed 78.1% retention at 100 cycles, the ZSCS-modified electrode also exhibited superior cycling durability, further validating the effectiveness of the self-assembled Cu NP layer in enhancing the full-cell reversibility and longevity. *Ex situ* SEM images provided direct evidence of the differences in Zn deposition behavior, as shown by Zn electrodes from NVO full cells after 100 cycles at 1 A g^{-1} (Fig. S17). The bare Zn anode displayed heterogeneous surface features, including deep pits and inactive domains, whereas the ZSCS electrode showed markedly uniform Zn deposition across the electrode surface. Compared to both bare Zn and CS electro-

des, the ZSCS modification thus ensures a more stable Zn/electrolyte interface in the full-cell system, aligning well with the enhanced reversibility observed in full-cell cycling.

Conclusions

In summary, this work presents an energy-efficient interfacial engineering strategy based on the self-assembly of Cu NPs on Zn anodes, enabled by a spontaneous galvanic replacement reaction and regulated by solubility equilibrium control. The engineered interfacial structure facilitates uniform Zn deposition, minimizes side reactions such as ZHS formation, and significantly improves cycling reversibility across a wide range of current densities. Moreover, the ZSCS interface can suppress spontaneous byproduct formation during the initial storage period after cell fabrication, an aspect that has received little attention but plays an important role in long-term stability. These insights not only provide a robust strategy for enhancing Zn anode reversibility but also contribute to the broader understanding of interfacial regulation in metal-based aqueous battery systems.

Author contributions

Jooyoung Jang: conceptualization, investigation, methodology, data curation, and writing – original draft. Yeonwoo Jeong: methodology, data curation, and writing – review & editing. Changshin Jo: conceptualization, funding acquisition, supervision, writing – original draft, and writing – review & editing.

Conflicts of interest

There are no conflicts to declare.

Data availability

All data supporting the findings of this study are available within the article and its supplementary information (SI). The SI includes the experimental section and additional characterization and electrochemical data, including SEM images, EDS mapping results, EIS spectra, contact angle measurement, linear sweep voltammetry results, chronoamperometric data, activation energy analysis, AFM images, and XRD patterns. See DOI: https://doi.org/10.1039/d6eb00014b.

Acknowledgements

This research was supported by the Korea Institute for Advancement of Technology (KIAT) grant funded by the Korean government (MOTIE) (RS-2024-00419413, HRD Program for Industrial Innovation) and the National Research Foundation of Korea (NRF) grant funded by the Korean government (MSIT) (RS-2024-00429941).

References

1 Y. Li, Z. Wang, Y. Cai, M. E. Pam, Y. Yang, D. Zhang, Y. Wang and S. Huang, *Energy Environ. Mater.*, 2022, **5**, 823.
2 M. Tang, Q. Liu, X. Zou, B. Zhang and L. An, *Adv. Mater.*, 2025, 2501361.
3 H. Ren, S. Li, B. Wang, Y. Gong, H. Zhang, J. Wang, Q. Lv, D. Wang, H. Liu and S. Dou, *Energy Storage Mater.*, 2024, **68**, 103364.
4 S. Adhikari, A. T. Sivagurunathan, M. Murmu and D.-H. Kim, *Korean J. Chem. Eng.*, 2024, **41**, 3647.
5 Y. Lv, Y. Xiao, L. Ma, C. Zhi and S. Chen, *Adv. Mater.*, 2022, **34**, 2106409.
6 C. Nie, G. Wang, D. Wang, M. Wang, X. Gao, Z. Bai, N. Wang, J. Yang, Z. Xing and S. Dou, *Adv. Energy Mater.*, 2023, **13**, 2300606.
7 S. Gull, C.-Y. Lai, W.-H. Lu, B. Rehman, W.-J. Chiu and H.-Y. Chen, *J. Mater. Chem. A*, 2024, **12**, 28919.
8 J. Jang, W.-G. Lim and C. Jo, *Batteries Supercaps*, 2024, **7**, e202400365.
9 W. Kang, I. Nam and C. Jo, *Korean J. Chem. Eng.*, 2023, **40**, 1353.
10 X. Liu, Y. Guo, F. Ning, Y. Liu, S. Shi, Q. Li, J. Zhang, S. Lu and J. Yi, *Nano–Micro Lett.*, 2024, **16**, 111.
11 Q. Zhao, X. Yu, J. Xue, M. Zhang, Z. Li, J. Wang, Y. Yang, Y. Zou, Y. Qiao and S.-G. Sun, *ACS Energy Lett.*, 2024, **9**, 4102.
12 W.-G. Lim, X. Li and D. Reed, *Small Methods*, 2024, **8**, 2300965.
13 R. Zhao, Y. Yang, G. Liu, R. Zhu, J. Huang, Z. Chen, Z. Gao, X. Chen and L. Qie, *Adv. Funct. Mater.*, 2021, **31**, 2001867.
14 Z. Yi, G. Chen, F. Hou, L. Wang and J. Liang, *Adv. Energy Mater.*, 2021, **11**, 2003065.
15 C. Zhou, Z. Zhang, M. Zhang, X. Sun, J. Zhang, G. Huang and Z. Na, *Energy Environ. Sci.*, 2025, **18**, 3817.
16 C. Li, A. Shyamsunder, A. G. Hoane, D. M. Long, C. Y. Kwok, P. G. Kotula, K. R. Zavadil, A. A. Gewirth and L. F. Nazar, *Joule*, 2022, **6**, 1103.
17 H. Qiu, X. Du, J. Zhao, Y. Wang, J. Ju, Z. Chen, Z. Hu, D. Yan, X. Zhou and G. Cui, *Nat. Commun.*, 2019, **10**, 5374.
18 Q. Nian, X. Luo, D. Ruan, Y. Li, B.-Q. Xiong, Z. Cui, Z. Wang, Q. Dong, J. Fan, J. Jiang, J. Ma, Z. Ma, D. Wang and X. Ren, *Nat. Commun.*, 2024, **15**, 4303.
19 X. Miao, J. Bao, S. Li, C. He, Z. Guo and Y. Wang, *EES Batteries*, 2026, **2**, 270–281.
20 M. Chen, R. Chen, I. Zhitomirsky, G. He and K. Shi, *Mater. Sci. Eng., R*, 2024, **161**, 100865.
21 M. Chen, L. Gong, I. Zhitomirsky and K. Shi, *Energy Environ. Sci.*, 2025, **18**, 4460.
22 J. Lei, Y. Yao, Z. Wang and Y.-C. Lu, *Energy Environ. Sci.*, 2021, **14**, 4418.

23 K. Zhao, C. Wang, Y. Yu, M. Yan, Q. Wei, P. He, Y. Dong, Z. Zhang, X. Wang and L. Mai, *Adv. Mater. Interfaces*, 2018, **5**, 1800848.
24 H. He, H. Tong, X. Song, X. Song and J. Liu, *J. Mater. Chem. A*, 2020, **8**, 7836.
25 H. Yang, Y. Qiao, Z. Chang, H. Deng, P. He and H. Zhou, *Adv. Mater.*, 2020, **32**, 2004240.
26 H. Yang, Z. Chang, Y. Qiao, H. Deng, X. Mu, P. He and H. Zhou, *Angew. Chem., Int. Ed.*, 2020, **59**, 9377.
27 Y. Q. Zheng, P. X. Sun, X. Y. Zhang, N. W. Li, L. Wu, D. Luan, X. Zhang, X. W. Lou and L. Yu, *Adv. Mater.*, 2024, **36**, 2405906.
28 X. Zhou, B. Wen, Y. Cai, X. Chen, L. Li, Q. Zhao, S.-L. Chou and F. Li, *Angew. Chem., Int. Ed.*, 2024, **63**, e202402342.
29 M. Fayette, H. J. Chang, X. Li and D. Reed, *ACS Energy Lett.*, 2022, **7**, 1888.
30 R. Li, Y. Du, Y. Li, Z. He, L. Dai, L. Wang, X. Wu, J. Zhang and J. Yi, *ACS Energy Lett.*, 2023, **8**, 457.
31 L. Wang, W. Huang, W. Guo, Z. H. Guo, C. Chang, L. Gao and X. Pu, *Adv. Funct. Mater.*, 2022, **32**, 2108533.
32 X. Zhu, W. Zhang, Z. Peng, L. Pan, B. Li, Z. Zhang, J. Zhu, W. Meng, L. Dai, L. Wang and Z. He, *Chem. Eng. J.*, 2024, **499**, 156521.
33 B. Li, K. Yang, J. Ma, P. Shi, L. Chen, C. Chen, X. Hong, X. Cheng, M.-C. Tang, Y.-B. He and F. Kang, *Angew. Chem., Int. Ed.*, 2022, **61**, e202212587.
34 I. Ohno, *Mater. Sci. Eng., A*, 1991, **146**, 33.
35 H. Cheng, C. Wang, D. Qin and Y. Xia, *Acc. Chem. Res.*, 2023, **56**, 900.
36 V. L. Filippov, A. V. Shapagin and A. V. Rudnev, *J. Electroanal. Chem.*, 2024, **965**, 118372.
37 A. V. Markin and N. E. Markina, *J. Chem. Educ.*, 2019, **96**, 1438.
38 J. Peng, B. Chen, Z. Wang, J. Guo, B. Wu, S. Hao, Q. Zhang, L. Gu, Q. Zhou, Z. Liu, S. Hong, S. You, A. Fu, Z. Shi, H. Xie, D. Cao, C.-J. Lin, G. Fu, L.-S. Zheng, Y. Jiang and N. Zheng, *Nature*, 2020, **586**, 390.
39 B. Liu, S. Wang, Z. Wang, H. Lei, Z. Chen and W. Mai, *Small*, 2020, **16**, 2001323.
40 G. Liang, J. Zhu, B. Yan, Q. Li, A. Chen, Z. Chen, X. Wang, B. Xiong, J. Fan, J. Xu and C. Zhi, *Energy Environ. Sci.*, 2022, **15**, 1086.
41 J. Kim, J. K. Seo, J. Song, S. Choi, J. Park, H. Park, J. Song, J.-H. Noh, G. Oh, M. H. Seo, H. Lee, J. M. Lee, I.-C. Jang, J. Kim, H.-J. Kim, J. Ma, J. Cho and J.-J. Woo, *Adv. Energy Mater.*, 2024, **14**, 2401820.
42 D. Yuan, W. Manalastas Jr., L. Zhang, J. J. Chan, S. Meng, Y. Chen and M. Srinivasan, *ChemSusChem*, 2019, **12**, 4889.
43 Z. Song, C. Yang, N. Kiatwisarnkij, A. Lu, N. Tunghathaithip, K. Lolupiman, T. Bovornratanaraks, X. Zhang, G. He and J. Qin, *ACS Appl. Mater. Interfaces*, 2024, **16**, 64834.
44 J. Song, S. Lee, Y. Kim, Y.-E. Sung, T. Yim and O. J. Kwon, *Korean J. Chem. Eng.*, 2024, **41**, 3027.
45 S. Chen, K. Ouyang, Y. Liu, H. Qin, M. Cui, A. Liu, Y. Wang, K. Zhang and Y. Huang, *Adv. Mater.*, 2025, **37**, 2417775.
46 J. N. Chazalviel, *Phys. Rev. A*, 1990, **42**, 7355.
47 S. Zheng, W. Zhao, J. Chen, X. Zhao, Z. Pan and X. Yang, *Nano–Micro Lett.*, 2023, **15**, 46.
48 J. Jang, J. Chun and C. Jo, *Energy Storage Mater.*, 2023, **62**, 102948.
49 P. Cao, X. Zhou, A. Wei, Q. Meng, H. Ye, W. Liu, J. Tang and J. Yang, *Adv. Funct. Mater.*, 2021, **31**, 2100398.
50 Y. Wang, Z. Deng, B. Luo, G. Duan, S. Zheng, L. Sun, Z. Ye, J. Lu, J. Huang and Y. Lu, *Adv. Funct. Mater.*, 2022, **32**, 2209028.
51 J. Huang, Y. Zhong, H. Fu, Y. Zhao, S. Li, Y. Xie, H. Zhang, B. Lu, L. Chen, S. Liang and J. Zhou, *Adv. Mater.*, 2024, **36**, 2406257.
52 Q. Li, A. Chen, D. Wang, Y. Zhao, X. Wang, X. Jin, B. Xiong and C. Zhi, *Nat. Commun.*, 2022, **13**, 3699.
53 H. Li, W. Jia, P. Chen, L. Wang, X. Yan and Y.-Y. Yang, *Appl. Surf. Sci.*, 2023, **607**, 155111.
54 J. Cao, H. Wu, Y. Yue, D. Zhang, B. Li, D. Luo, L. Zhang, J. Qin, X. Zhang and X. Yang, *J. Energy Chem.*, 2024, **99**, 671.
55 C. Tian, H. Wang, L. Xie, Y. Zhong and Y. Hu, *Adv. Energy Mater.*, 2024, **14**, 2400276.
56 H. Tian, G. Feng, Q. Wang, Z. Li, W. Zhang, M. Lucero, Z. Feng, Z.-L. Wang, Y. Zhang, C. Zhen, M. Gu, X. Shan and Y. Yang, *Nat. Commun.*, 2022, **13**, 7922.
57 Y.-H. Lee, Y. Jeoun, S.-H. Lee, J. H. Kim, S.-Y. Kim, S.-H. Yu, K.-S. Ahn and Y.-E. Sung, *Chem. Eng. J.*, 2023, **464**, 142580.
58 Y. Geng, W. Xin, L. Zhang, Y. Han, H. Peng, M. Yang, H. Zhang, X. Xiao, J. Li, Z. Yan, Z. Zhu and F. Cheng, *Natl. Sci. Rev.*, 2025, **12**, 397.
59 X. Hu, S. Gao, T. Lin, X. Peng, Y. Huang, Y. Zhang, X. Yang, L. Wang, G. Luo, Z. Wen, B. Johannessen, S. Wang, L. Wang and B. Luo, *Adv. Mater.*, 2025, 2416714.